Materials Advances

ROYAL SOCIETY OF CHEMISTRY

PAPER

View Article Online
View Journal | View Issue

Cite this: *Mater. Adv.*, 2025, **6**, 9556

A thorough and comprehensive study of novel phthaloperinone derivatives: from synthesis and property evaluation to applications in light-emitting diodes

Ana C. Amorim, *[a] Jorge Morgado, [b] João P. Prates Ramalho, [cd] Hugo Cruz, [ef] Carla Cunha, [a] José A. Paixão, [g] J. Sérgio Seixas de Melo, [a] Susana M. M. Lopes, [a] Luís C. Branco [f] and Anthony J. Burke *[ahi]

Despite its promising electronic and semiconducting properties, 12*H*-phthaloperin-12-one remains a largely unexplored molecule, with limited studies regarding the impact of structural modifications on its properties and its application in light-emitting devices. To address this gap, we report the synthesis of 12 novel phthaloperinone derivatives, designed to fine-tune the photophysical, electrochemical, thermal and electroluminescence properties through the incorporation of electron-donating and electron-withdrawing substituents. The majority of substituents was found to interfere with the electronic distribution in the phthaloperinone core during the electronic excitation process. The introduction of a triphenylamine unit, as in compounds **3f**/**4f**, resulted in the lowest energy gap of 2.22 eV, making this isomeric mixture a promising candidate for use as an organic semiconductor material. Electrochemical studies demonstrated that compounds **3e**/**4e**–**3h**/**4h** and **3l**/**4l** exhibited enhanced electrochemical stability, while thermal analysis showed that the pyrene-substituted derivative (**3e**/**4e**) displayed the highest thermal resistance (T_d = 458 °C). Organic light-emitting diodes were fabricated to evaluate their electroluminescence properties. Compounds **3l**/**4l**, which contain a phenyltriazolyl unit, achieved the best performance, displaying a maximum luminance of 99 cd m^{-2} at 7.5 V, a luminous efficiency of 0.014 cd A^{-1}, and a turn-on voltage of 3.3 V. These findings provide valuable insights into the structure–property relationships of phthaloperinone derivatives and highlight their potential for a wide range of applications, including electronic and optoelectronic devices.

Received 15th July 2025,
Accepted 24th October 2025

DOI: 10.1039/d5ma00761e

rsc.li/materials-advances

Introduction

Over the past decade, perylene diimide (PDI) and naphthalene diimide (NDI) chromophores have become benchmark materials in organic electronics, owing to their excellent optoelectronic properties.[1–7] Within organic electronics, their application has extended to organic light-emitting diodes (OLEDs), where reported devices can reach external quantum efficiencies (EQE) values of 0.06–5%, maximum luminances (L_{max}) ranging from 10^2–10^3 cd m^{-2} and a turn-on voltage (V_{on}) of around 2.6 V.[8–11]

Building on the success of these rylene diimides in organic electronics, perinone-based chromophores have recently emerged as attractive alternatives. Originally developed as robust industrial pigments,[12,13] their extended π-conjugation and structural similarity to PDI and NDI derivatives have highlighted their potential in organic electronics, particularly as *n*-type semiconductors in photovoltaic devices.[14–17] This increasing attention is supported by their synthetic simplicity (their methods are generally modular in nature and allow the introduction of diverse functionalities), strong visible

[a] *University of Coimbra, Coimbra Chemistry Center-Institute of Molecular Sciences (CQC-IMS) and Department of Chemistry, 3004-535, Coimbra, Portugal. E-mail: anacatarina.amorim@hotmail.com, ajburke@ff.uc.pt*
[b] *Department of Bioengineering and Instituto de Telecomunicações (IT), Instituto Superior Técnico, Universidade de Lisboa, 1049-001, Lisboa, Portugal*
[c] *Department of Chemistry and Biochemistry, School of Sciences and Technology, University of Évora, Rua Romão Ramalho 59, 7000-671, Évora, Portugal*
[d] *HERCULES Laboratory, IN2PAST—Associate Laboratory for Research and Innovation in Heritage, Arts, Sustainability and Territory, University of Évora, 7000-809, Évora, Portugal*
[e] *INL–International Iberian Nanotechnology Laboratory, Avenida Mestre José Veiga, 4715-330, Braga, Portugal*
[f] *LAQV-REQUIMTE, Department of Chemistry, NOVA School of Science and Technology, NOVA University of Lisbon, 2819-516, Caparica, Portugal*
[g] *University of Coimbra, CFisUC, Department of Physics, Coimbra, 3004-516, Portugal*
[h] *Faculty Pharmacy, University of Coimbra, Pólo das Ciências da Saúde, 3000-548, Coimbra, Portugal*
[i] *Center for Neurosciences and Cellular Biology (CNC), Faculdade de Medicina da Universidade de Coimbra, 3004-504, Coimbra, Portugal*

light absorption, high fluorescence quantum yields (φ_F) (up to 51%), and exceptional photochemical and thermal stability.[18–20]

Despite these promising characteristics, reports exploring perinone derivatives in OLEDs devices are extremely scarce. Within this class of chromophores, 12*H*-phthaloperin-12-one, also known as phthaloperinone or Solvent Orange 60, is the only example reported as a promising material for organic electroluminescent devices, mentioned in a patent from the 1990s, which, unfortunately, does not include any detailed device performance data.[21] This lack of studies strongly contrasts with the extensive research on PDI- and NDI-based materials, highlighting the absence of similar investigations on perinone-type systems and the need to explore their potential in light-emitting applications.

While its use in OLEDs remains unexplored, the intrinsic photophysical and electrochemical properties of phthaloperinone have been studied, revealing intramolecular charge transfer (ICT) behaviour and an estimated HOMO–LUMO gap below 3 eV, suggesting potential semiconducting behaviour.[18–20] In addition to these intrinsic properties, this compound has also demonstrated potential in other areas. For instance, it has been investigated as a fluorescence probe with a "switch-off" behaviour in response to Cu^{2+} ions, highlighting its potential for the development of sensing materials.[22] Moreover, a recent study by Palmer *et al.* explored access to the triplet state of this

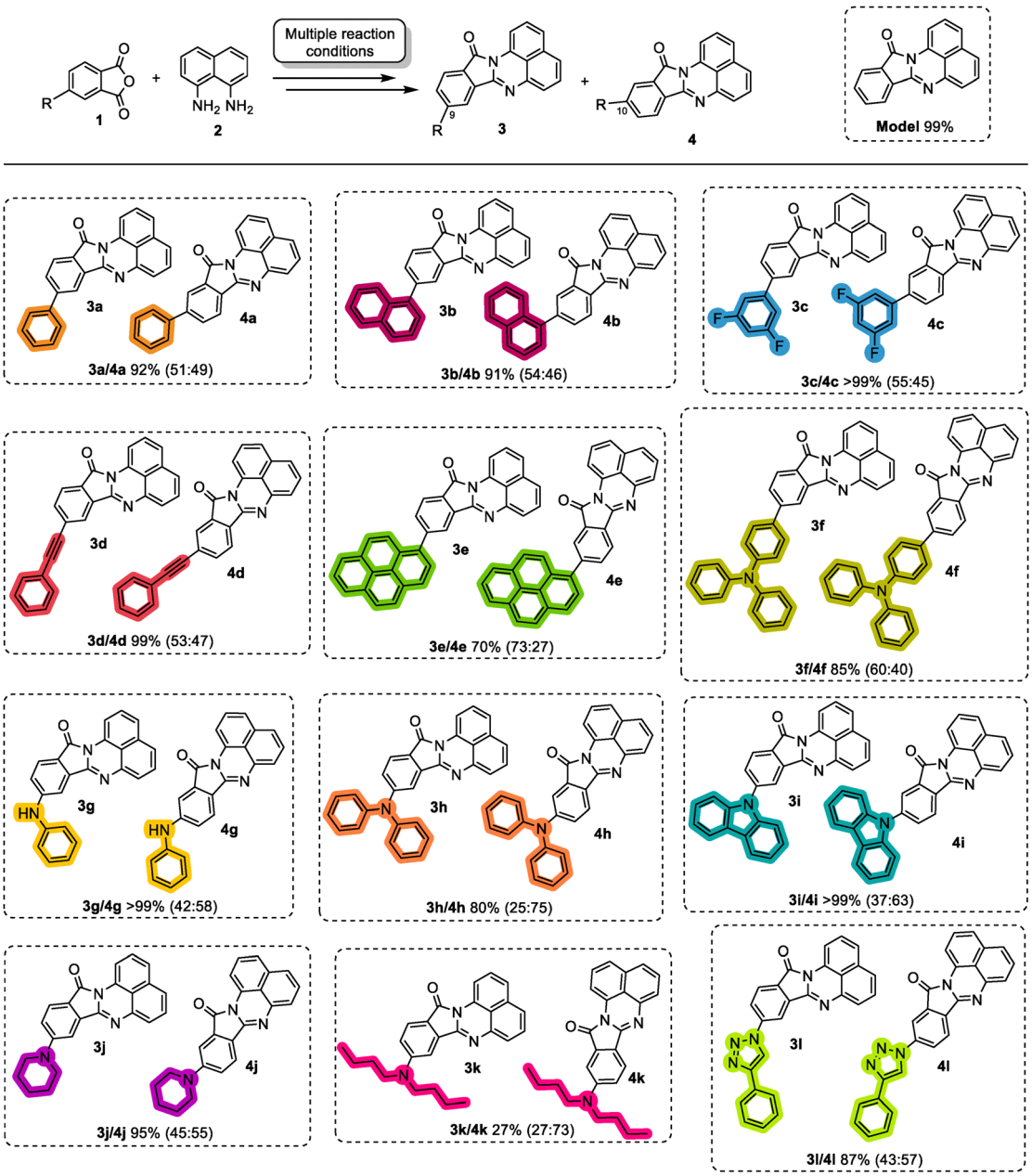

Fig. 1 Overall synthetic pathway leading to the target phthaloperinones (**3a**/**4a**–**3l**/**4l**) with corresponding yields and isomeric ratio (**3** : **4**).

structure without using a transition metal, by simply replacing the C═O group with a C═S moiety. This modification enables its use as a metal-free triplet photosensitizer, with potential applications in photodynamic therapy, photocatalysis and solar energy conversion.[23]

This limited research on phthaloperinones presents a unique opportunity to explore this understudied class of compounds in light-emitting devices. Furthermore, the possibility of fine-tuning their properties through strategic molecular design by introducing electron-donating and electron-withdrawing substituents remains largely unexplored. Such structural modifications are key tools for adjusting energy levels, improving charge transport, and optimizing optoelectronic performance, thereby broadening the potential of these materials across organic electronic devices, including organic field-effect transistors (OFETs), organic photovoltaics (OPVs), and OLEDs.[24,25]

To address this opportunity, and taking into consideration the promising electrochemical and photophysical properties of these compounds reported in previous literature, the present study reports the synthesis of novel phthaloperinone derivatives, along with the unsubstituted phthaloperinone, aiming to explore how different substituent groups influence their properties. The effects of substitution on their photophysical, electrochemical, and thermal properties were systematically evaluated. Additionally, theoretical calculations were also performed to help correlating molecular structure and properties. Finally, these newly synthesized structures were used to fabricate simple OLED devices in order to assess their electroluminescence properties.

Results and discussion

Synthesis

Fig. 1 illustrates the general synthetic route leading to the final phthaloperinones (**3a**/**4a**–**3l**/**4l**), which involves one to three steps. Although phthaloperinones can be synthesized *via* a solvent-free ''green'' condensation process by heating solid phthalic anhydrides and naphthalene-1,8-diamines,[18,20] the best results in this study were obtained using boiling acetic acid (AcOH). The reaction of monosubstituted phthalic anhydrides resulted in the formation of regioisomers **3** and **4**, bearing different substituents (**a-l**) at the 9- or 10-positions of the phthaloperinone core (Fig. S1–S64, SI). These isomers could not be isolated by traditional separation methods such as column chromatography, selective crystallization or solubility-based separation methods. Furthermore, high performance liquid chromatography (HPLC) analysis showed that their retention times are extremely close (Fig. S65–S79, SI), limiting the study to isomeric mixtures.

However, in a few cases, after several preparative TLC plates, a few milligrams of the regioisomers **3b**, **4b**, **3g**, and **4g** were successfully separated, as shown in Fig. 2. With these small quantities, it was possible to perform 1D and 2D NMR experiments to confirm the structure of each isomer and conduct photophysical and electrochemical studies, enabling the study

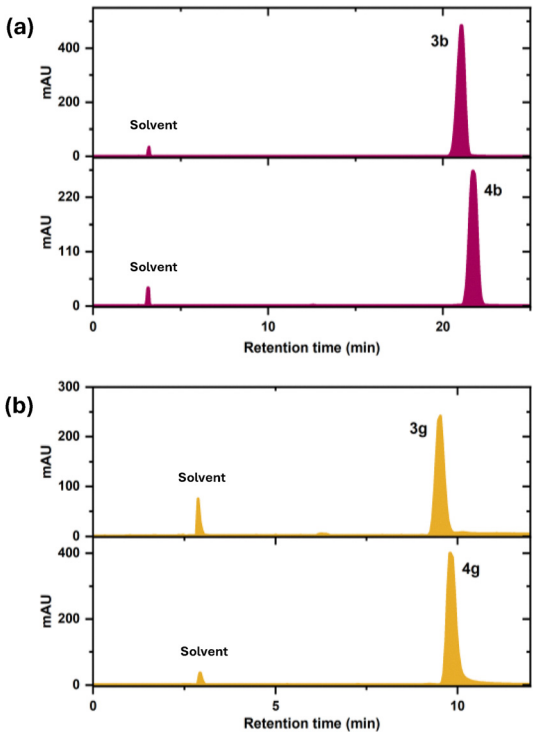

Fig. 2 HPLC chromatogram of isolated regioisomers (a) **3b** and **4b** and (b) **3g** and **4g**.

of their isolated properties. The heteronuclear multiple bond correlation (HMBC) spectra (Fig. S22, S25 and S47, SI) indicated that compounds **3b** and **3g** correspond to regioisomers with the substituent at the 9-position, while **4b** and **4g** bear the substituent at the 10-position. Based on this, we assume that in all other isomeric mixtures, the **3**-series isomers correspond to phthaloperinones with substituents at the 9-position, while the **4**-series isomers correspond to phthaloperinones with substituents at the 10-position.

Different substituent groups, including electron-withdrawing (**3c**/**4c** and **3l**/**4l**) and electron-donating (**3a**/**4a**, **3b**/**4b** and **3d**/**4d**–**3k**/**4k**) groups, were introduced to assess their impact on the ICT, as well as on their photophysical, electrochemical, thermal and electroluminescence properties. The introduction of these substituents involved a rich variety of chemical reactions including nucleophilic substitution and click reactions, as well as Suzuki–Miyaura, Buchwald–Hartwig and Sonogashira cross-coupling reactions.

The analysis of the substitution patterns in the **3**- and **4**-series of regioisomers reveals a general trend: compounds bearing strong electron-donating groups (**3g**/**4g**, **3h**/**4h**, **3i**/**4i**, **3j**/**4j** and **3k**/**4k**) with the exception of compounds **3f**/**4f** tend to produce slightly higher proportions of the 4-isomer, whereas those containing electron-withdrawing substituents (**3c**/**4c** and **3l**/**4l**), as well as weakly donating groups, including compounds **3a**/**4a**, **3b**/**4b** and **3d**/**4d** yielded approximately equimolar mixtures of both isomers. These observations suggest that electronic factors play a major role, as strong electron-donating groups enhance charge delocalization, slightly stabilizing one

regioisomer over the other. Bulkier aromatic groups such as pyrene (**3e**/**4e**) and triphenylamine (**3f**/**4f**) tended to favour the formation of the isomer **3** likely due to steric hindrance affecting the approach of the reacting species.

In general, the final compounds (**3a**/**4a**–**3l**/**4l**) were obtained in very good yields (up to >99% yield) using simple purification methods, typically involving *n*-hexane washes or short chromatographic columns. All the compounds exhibit colouration ranging from orange to reddish, as depicted in Fig. S80 (SI). All experimental procedures and characterization data related to the synthesis are provided in the SI.

X-ray crystallography

A single-crystal X-ray diffraction (XRD) study of compound **3b** was performed at room temperature. Details of the data collection, solution and least-squares refinement of the structure are provided in the SI. A summary of the crystallographic data for compound **3b** is presented in Table S1 (SI).

Compound **3b** crystallizes in the centric monoclinic space group $P21/c$ (nb. 14) with cell parameters a = 14.882(2) Å, b = 6.2974(9) Å, c = 21.093(3) Å, β = 101.747(8)°, and one symmetry-independent molecule (Z = 4, Z' = 1) per unit cell. An ORTEP of the molecule is shown in Fig. 3, that fully confirms the expected molecular configuration based on the NMR studies. Bond distances and angles of the molecule are unexceptional. The most relevant ones are provided in Table S2 (SI). It is noteworthy to point out the short C7–N2 bond correlating with a significant double-bond character. All rings in the structure are planar with maximum deviation from the least-squares plane of 0.06 Å, and rms deviation of 0.03 Å for the core moiety and 0.08 Å (max), 0.006 Å (rms) for the naphthalene substituent, respectively. The angle between the least-squares planes of the molecule core and that of the naphthalene substituent is 70.63(3)° (Fig. S81 and Table S2, SI). The crystal structure does not feature classical hydrogen bonds, but a weak intramolecular C12–H12···O1 interaction can be spotted with a C12···O1 distance of 2.969(2) Å and C12–H12···O1 angle of 122°. A view of the molecular packing is shown in Fig. 4. The CIF containing the crystallographic data for compound **3b** was deposited at the Cambridge Crystallographic Data Centre, with reference CCDC 2423273.

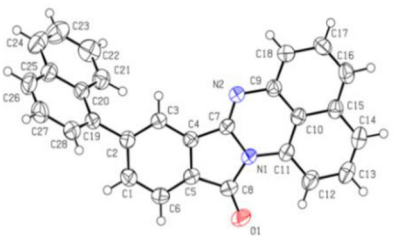

Fig. 3 ORTEP drawing depicting the molecule of **3b**. The anisotropic displacement ellipsoids are drawn at the 50% probability level.

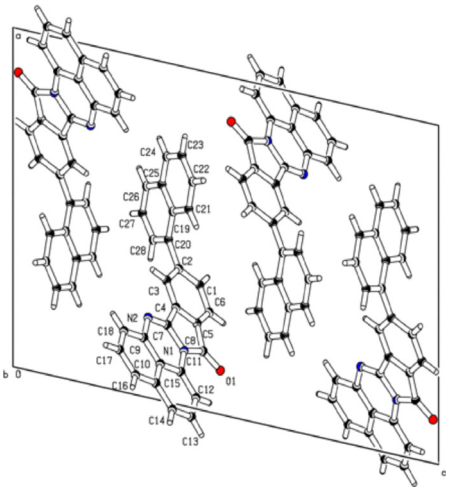

Fig. 4 View of the molecular packing of compound **3b** along the crystallographic *b*-axis.

Theoretical calculations

Density functional theory (DFT) and time-dependent density functional theory (TD-DFT) were employed to characterise compounds' ground- and excited-state. All calculations were performed using the Gaussian software suite.[26] All details of DFT calculations are provided in the SI.

The Frontier molecular orbitals (FMOs) of the compounds are illustrated in Fig. S83 (SI). For most of the compounds, the HOMO resembles that of the model compound, being primarily localized on the perimidine moiety, whereas the LUMO is mainly distributed over the isoindolinone moiety.

Fig. 5 illustrates the change in the electron density that occurs in the **Model** compound and pure isomers of the synthesised compounds when they are electronically excited (lowest energy excitation). Fig. S82 (SI) shows the corresponding changes for all the compounds. The difference between the electronic densities of the states involved in the transitions, $\Delta\rho(r)$, is depicted, clearly revealing the regions of the compounds that lose or gain electron density upon that electronic excitation. The major electronic rearrangement is restricted to the phthaloperinone core for all the compounds, resembling the rearrangement that occurs in the **Model** compound, with particular features depending on the nature of the attached substituent group. The electronic relocation in the **Model** compound (Fig. 5) reveals a clear charge transfer from the perimidine moiety to the isoindolinone moiety, which is consistently observed across all compounds. This charge density redistribution evidences the ICT character of the electronic excitation.

The compounds with phenyl (**3a**/**4a**), naphthalene (**3b**/**4b**) and pyrene (**3e**/**4e**) aromatic units attached at the 9- and 10-positions of phthaloperinone do not present any visible change of charge density at the aromatic substituents indicating a limited participation of these aromatic units on the electronic excitation process, and therefore a limited participation in the

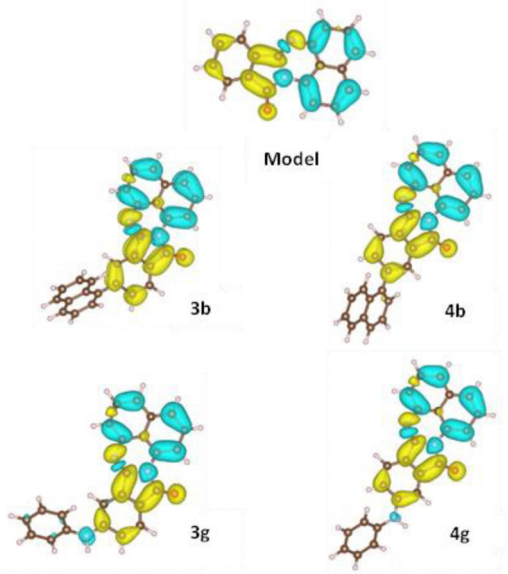

Fig. 5 Optimized molecular geometries for the **Model** compound and isolated regioisomers **3b**, **4b**, **3g** and **4g**. Contour plots of the electron density difference $\Delta\rho(r)$ for the lowest energy excitation are also shown, where yellow indicates an increase in electron density, while blue represents a depletion of electron density Frontier molecular orbital distributions for **Model** compound and isolated regioisomers **3b**, **4b**, **3g** and **4g**.

FMOs involved in the lowest energy excitation. This result was expected specially for compound **3b**, since the dihedral angle of 70.63° between the core and the naphthyl substituent, as verified in the X-ray crystallography, probably contributes to the limited electronic interaction between them, thereby hindering the involvement of the aromatic substituent in the electronic excitation process. An interesting case is represented by compounds **3e**/**4e**, for which the S_1 state shows a more complex configuration. Although the HOMO and HOMO−1 extend over the pyrene moiety, similar contributions are found in the LUMO+1, which participates in the excitation. Consequently, the resulting electron density difference is closely comparable to that of the model compound.

For compounds **3d**/**4d**, bearing the phenylacetylene electron withdrawing group, an increase in electronic charge is visible in this unit upon excitation (Fig. S82, SI), which is expected on geometrical grounds due to its linear conjugated system. For the compounds bearing strong electron-donating groups (**3f**/**4f** (triphenylamine), **3g**/**4g** (phenylamine), **3h**/**4h** (diphenylamine), **3i**/**4i** (carbazole), **3j**/**4j** (piperidine), and **3k**/**4k** (dibutylamine)) the HOMO extends over the attached substituents (Fig. S83, SI), and a reduction in electron density on these groups is expected upon excitation. That is clearly visible in compounds **3g**/**4g**, **3i**/**4i**, **3j**/**4j**, **4h**, strongly evident on **3h**, and only slightly noticeable in **3k** (due to the aliphatic nature of this group and lack of a π-system, which is the anti-thesis to **3h** that has a very extended π-system (diphenylamine)). The same electron donor effect of the triphenylamine is observed for **3f**, but when this group is at the 10-position, in **4f**, a slight electron acceptor character is inferred from the DFT calculations, as there is a small increase of the electron density in the group when the compound is excited. For the compounds bearing electron-withdrawing substituents (difluorophenyl in **3c**/**4c** and phenyltriazolyl in **3l**/**4l**) the LUMO extends toward the pendant groups (Fig. S83, SI), resulting in increased electron density on these substituents upon excitation, particularly in **4c** and **4l** (Fig. S82, SI).

The ICT characterization index (Δr index) (Table S3, SI) was used to quantify the charge transfer distance and classify the nature of these electronic transitions.[27] A high Δr index indicates a strong ICT character, with transitions typically classified as ICT when exceeding the widely accepted threshold of 2.0 Å. Based on this criterion, most S_1 excitations, including that of the **Model** compound, can be identified as ICT. The exceptions are compounds **3h**/**4h**, **3i** and **3j**/**4j**. For these compounds, all with strong electron-donor groups, there is an important electronic flux from both extremes of the molecule toward the centre thus resulting in a smaller Δr value. For the rest of the compounds, with electron-withdrawing groups, the electron displacement is unidirectional resulting in a higher Δr value. In particular, for the compounds **3c**/**4c**, **3d**/**4d**, **3f**/**4f** and **3l**/**4l** the index value is much larger, thus indicating a larger displacement distance of the charge upon excitation.

The oscillator strength and the absorption wavelengths of key transitions for the compounds in dichloromethane were calculated (Table S3, SI). The simulated absorption spectra for the successfully isolated regioisomers **3b**, **4b**, **3g**, and **4g**, along with their comparison to the experimental spectra, are presented in the photophysical properties section. Additionally, for these isomers, the geometric optimization of the first excited electronic state (S_1) and vertical emission calculations were performed.

The calculated HOMO–LUMO gaps (Fig. 6) are similar to that of the **Model** compound and remain largely unaffected by the substituents. In most cases, the HOMO energy is only slightly influenced by substitution. Notable destabilization is observed in compounds **3f**/**4f** and **3j**/**4j**, and to a lesser extent in **3g**/**4g** and **3k**/**4k**, all of which bear strong electron-donating groups. In these compounds, the HOMO extends over the

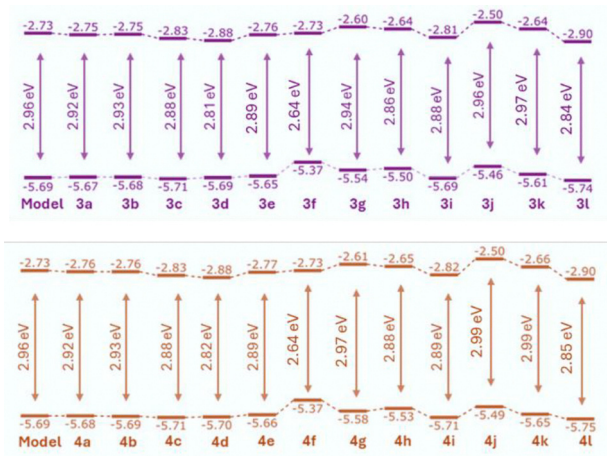

Fig. 6 Calculated energy levels for all compounds.

attached substituents (Fig. S83, SI), with the increased electron density on these donor groups leading to the observed HOMO destabilization, consistent with the general effect of electron-donating substituents on Frontier orbital energies. For the **3j**/**4j** compounds, the LUMO levels energy increase as observed for the corresponding HOMO energies, maintaining an unchanged energy gap. However, in the case of **3f**/**4f**, the LUMO levels remain unaffected relative to the **Model** compound, while the HOMO energies increase, leading to a significant energy gap (E_{gap}) reduction. This reduction makes **3f**/**4f** promising candidates for use as organic semiconductor materials. In general, all compounds exhibit E_{gap} below 3 eV, which suggests favourable optoelectronic properties. However, the results of these calculations performed at the single molecule are likely to differ of the properties in solid-state, due to the interactions between the molecules, influenced by their packing.

Photophysical properties

Absorption and fluorescence emission spectra, fluorescence quantum yields (ϕ_F), and time-resolved fluorescence measurements (τ_F) were acquired for all isomeric mixtures, including isolated isomers **3b**, **4b**, **3g** and **4g**. These measurements were taken in solvents of varying polarities such as toluene (ε = 2.379), DCM (ε = 8.93) and DMF (ε = 36.71) and in the solid-state (powder). The photophysical parameters are presented in Fig. 7 and 8, Tables S4–S7 and Fig. S84–S89 (SI). **Model** compound was included for comparison.

Solvent polarity, in general, had a slight effect on the spectral properties. Increasing the solvent polarity (in the order: toluene, DCM and DMF), led to either red and blue shifts of the maximum absorption spectra (λ_{max}^{abs}) depending on the substituent. The maximum emission peaks (λ_{max}^{em}) consistently red-shifted (~2–16 nm) with increasing solvent polarity for all compounds (Tables S4 and S5 and Fig. S84 and S85, SI). As shown in Fig. 7(b), when weak electron-donor groups are attached to the phthaloperinone (such as in compounds **3a**/**4a**, **3b**/**4b** and **3e**/**4e**), the shape and position of the absorption peaks are relatively similar to those of the **Model** compound. The introduction of phenyl (**3a**/**4a**), naphthalene (**3b**/**4b**) and pyrene (**3e**/**4e**) as phthaloperinone substituents caused minimal spectral shifts, indicating that these aromatic substituents remain electronically decoupled from the core. This is presumably mainly due to the deviation from coplanarity as evidenced in **3b**, and gratifyingly, this observation aligns with the DFT findings. The introduction of a phenylacetylene group (**3d**/**4d**) caused a slight redshift of both absorption and emission spectra (Fig. 7(b)) as expected from the previous discussion on the DFT calculations. This result is consistent with the DFT-calculated HOMO–LUMO gap, which is lower for compounds **3d**/**4d** (2.81/2.82 eV) when compared to the other weak donor-substituted compounds (**3a**/**4a**, **3b**/**4b** and **3e**/**4e**). In this compound, the LUMO extends over the phenylacetylene substituent (Fig. S83, SI), leading to a decrease in LUMO energy. This delocalization enhances the electronic coupling between the phenylacetylene group and the phthaloperinone core, resulting in reduced HOMO–LUMO gap and suggesting partial charge-transfer character in the electronic excitation. For moderate to strong electron-donor groups (Fig. 7(c)), the presence of nitrogen atoms in the substituents leads to slight changes in the overall spectroscopic properties. These changes are more

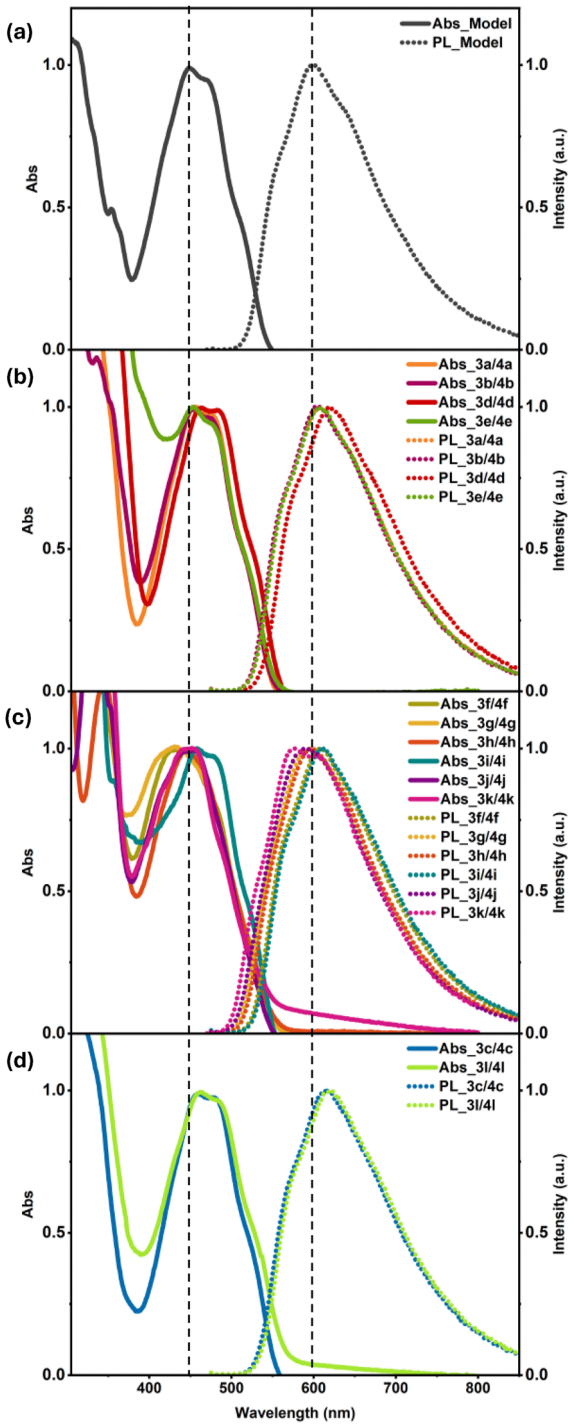

Fig. 7 Absorption and fluorescence emission spectra for all compounds in DCM. (a) **Model** compound; (b) phthaloperinones with weak electron-donor groups; (c) phthaloperinones with moderate and strong electron-donor groups; (d) phthaloperinones with electron withdrawing groups. The vertical dashed lines are aligned with the maximum absorption and maximum emission of the **Model** compound.

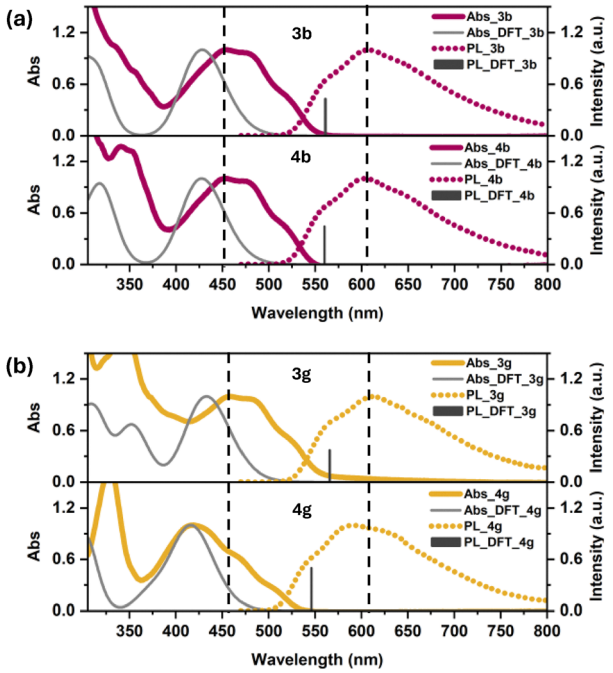

Fig. 8 Absorption (solid lines) and fluorescence emission spectra (dot lines) for compounds (a) **3b** and **4b** and (b) **3g** and **4g** in DCM. DFT absorption spectra (light grey lines) and maximum emissions (dark grey vertical lines) were included in all graphs.

evident for compounds **3f**/**4f** and **3k**/**4k**. The introduction of triphenylamine (**3f**/**4f**) and phenylamine (**3g**/**4g**) units caused notable blue shifts in the absorption spectra leading to an increase of Stokes shift (Δ_{ss}) of approximately 1000 to 2000 cm^{-1} (depending on the solvent), relative to the other derivatives. Again, the DFT results corroborate this experimental data. For phthaloperinones with electron-withdrawing groups (as difluorophenyl in **3c**/**4c** and phenyltriazolyl in **3l**/**4l**), in Fig. 7(d), the shapes of absorption and emission spectra are very similar, but both λ_{max}^{abs} and λ_{max}^{em} showed a red-shift when compared to the **Model** compound.

The spectra of isolated compounds **3b**, **4b**, **3g** and **4g** in DCM (Fig. 8(a) and (b), respectively) show that for weak electron-donor groups (in the case of **3b** and **4b**, with a naphthalene unit at the 9- and 10-positions, respectively), both absorption and emission spectra are nearly identical. However, when a strong electron donor group is present (as in **3g** and **4g**) both spectra differ considerably. While compound **3g** maintains the same profile of λ_{max}^{abs} and λ_{max}^{em} near to the maxima of the **Model** compound, compound **4g** shows completely different shapes and blue shifted λ_{max}^{abs} and λ_{max}^{em}. These differences are more evident in the absorption spectra. This behavior can be rationalized by the fact that, in compounds **3b**/**4b**, the Frontier orbitals do not extend over the attached group (Fig. S83, SI). Consequently, the electronic system involved in the excitation is confined to the core moiety, which is identical in both isomers. In contrast, the situation is different for the **3g**/**4g** pair. Compared to compound **3g**, in compound **4g** the Frontier orbitals, particularly the HOMO, extend substantially over the phenylamine group. In the same figure (Fig. 8), the simulated absorption spectra and vertical emission calculations for the isolated regioisomers **3b**, **4b**, **3g**, and **4g** are also shown, exhibiting trends consistent with the experimental data, despite significant deviations in the predicted absorption and emission maxima.

In solid-state (powder) measurements, all compounds showed a red-shifted λ_{max}^{abs} (6–69 nm) when compared with the **Model** compound, with the exception of compounds **3f**/**4f** (see detail data in Table S6 and Fig. S86, SI). On the other hand, all compounds showed a blue-shift in the λ_{max}^{em}, except the isolated isomer **4g**. Compounds **3c**/**4c** and **3i**/**4i** had the largest shifts in λ_{max}^{em} and λ_{max}^{abs}, respectively, resulting in Δ_{ss} two times higher than the **Model** compound. Some differences were observed in λ_{max}^{em} between the isolated isomers **3b** and **4b**, and **3g** and **4g**, though in solid-state, these isolated isomers displayed more similar behaviour. Compounds **3k**/**4k** were not tested due to its oil-like consistency.

In general, solution fluorescence quantum yields (ϕ_F) ranged between 2 and 8%, decreasing as solvent polarity increases for all compounds (Table S5, SI). The solid-state (powder) fluorescence quantum yields were generally lower than those in solution, with compounds **3f**/**4f**, **3i**/**4i** and **3l**/**4l** presenting the lowest ϕ_F values ($\sim 10^{-3}$), in contrast with the other compounds ($\sim 10^{-2}$) (Table S6, SI). In both solution and solid-state studies, the fluorescence lifetimes (τ_i) are found mono-exponential for all compounds and range from 320 to 1300 ps (see Tables S5 and S6, SI). In solution, the k_{NR}/k_R ratio varies from 12 to 58, whereas in solid-state this ratio was between 30 and 199 times (Fig. S88, SI), indicating that non-radiative decay processes dominate over the radiative processes in both conditions.

Additionally, all isomeric mixtures, except **3k**/**4k** due to its oil-like texture, were deposited by vacuum deposition on glass substrates and Spectrosil, allowing the measurement of the absorbance in films (Fig. S89 and S90, SI). As shown in Table S7 (SI), for all compounds, the λ_{max}^{abs} of the films were red-shifted when compared to the λ_{max}^{abs} in solution (DCM) and blue-shifted when compared to the λ_{max}^{abs} in powder. We attribute this behaviour to the different intermolecular interactions, such as van der Waals, hydrogen bonding, and possibly π–π interactions. The variation in the absorption spectra of thin films of phthaloperinone derivatives upon aging was also studied (Fig. S90, SI), indicating that compounds **3b**/**4b**, **3f**/**4f** and **3l**/**3l** are by far the most stable compounds in film form, even when exposed to air.

Electrochemical properties

The electrochemical properties of all prepared phthaloperinones, including the isolated regioisomers, were studied in DCM solutions using cyclic voltammetry (CV). In CV voltammograms (Fig. S91 and S92 and Table S8, SI), all phthaloperinones showed an oxidation/reduction process in the positive potential range and a reduction/oxidation process in the negative potential range, suggesting their ability to sustain both electron and hole transport.[28] The HOMO and LUMO energy levels were

Table 1 Thermal and electrochemical properties

Compounds	T_d[a]/T_m[b] (°C)	HOMO (eV)[c]	LUMO (eV)[c]	Energy gap (eV)[d]
Model	285.1/225.5	−5.58	−3.15	2.43
3a/**4a**	330.6/207.6	−5.57	−3.19	2.38
3b/**4b**	354.7/179.1	−5.61	−3.23	2.38
3c/**4c**	365.5/221.2	−5.58	−3.18	2.40
3d/**4d**	372.4/217.7	−5.63	−3.23	2.40
3e/**4e**	458.0/292.9	−5.64	−3.23	2.41
3f/**4f**	260.3/—[e]	−5.30	−3.08	2.22
3g/**4g**	386.1/261.2	−5.46	−3.07	2.39
3h/**4h**	309.7/220.9	−5.51	−3.10	2.41
3i/**4i**	200.0/—[e]	−5.65	−3.35	2.30
3j/**4j**	243.1/167.6	−5.46	−3.06	2.40
3k/**4k**	257.2/—[f]	−5.42	−3.18	2.24
3l/**4l**	285.9/212.5	−5.63	−3.30	2.33
3b	nd	−5.61	−3.18	2.43
4b	nd	−5.59	−3.20	2.39
3g	nd	−5.44	−3.08	2.36
4g	nd	−5.44	−3.02	2.42

[a] Temperature of 5% weight loss. [b] Melting temperature. [c] HOMO/LUMO calculated from the first oxidation and first reduction onset potentials, respectively. [d] |HOMO–LUMO|. [e] No events were observed. [f] Not determined.

determined from the onsets of the first oxidation and first reduction potentials, respectively. All relevant data can be found in Table 1 and Table S8 (SI).

In general, all compounds exhibit reversible reduction behaviour in the negative potential range. However, only compounds **3e**/**4e**, **3f**/**4f**, **3g**/**4g**, **3h**/**4h** and **3l**/**4l** show reversible oxidation behaviour in the positive potential range, indicating that pyrene, triphenylamine, phenylamine, diphenylamine and phenyltriazolyl substituents, respectively, enhance electrochemical stability.

Multi-scan CV was performed for some of the compounds (Fig. S93, SI), demonstrating that compounds **3a**/**4a**, **3e**/**4e** and **3h**/**4h** exhibit some electrochemical stability in the positive potential range, although a slight appearance of new species is observed. In contrast, for compounds **3b**/**4b**, **3d**/**4d**, **3j**/**4j** and **3l**/**4l** the main anodic peaks completely disappear with an increasing number of scans, indicating that they are not electrochemically stable. The appearance of new species between 0.25 and 1 V is common in most of our compounds. We believe that these new species are dimers formed during the electrooxidation reaction.[29]

The HOMO and LUMO energy levels, as well as the energy gaps, are very similar for all the compounds, even when compared with the unsubstituted phthaloperinone (**Model** compound) (Table 1). However, and in agreement with the results obtained from theoretical calculations, compounds **3f**/**4f** showed an increased HOMO level compared to the other compounds, and the lowest energy gap (2.22 eV). In fact, the low energy gaps demonstrated by all compounds highlight their potential semiconductive properties.

It is also worth noting that, although the substituents have small contributions to the electronic transitions or charge distributions, which is a clear indication that both the HOMOs and the LUMOs are primarily localized in the core of phthaloperinones (as also verified by DFT studies), they have some influence on the electrochemical stability of the structure.

Thermal stability

Thermogravimetric analysis (TGA) and differential scanning calorimetry (DSC) studies were performed to investigate the thermal stability of these emitters. These studies are essential, as thermal deposition under vacuum during OLED fabrication requires materials with good thermal properties.

As shown in Table 1 and Fig. S94 (SI), compounds **3a**/**4a**–**3e**/**4e**, **3g**/**4g** and **3h**/**4h** have the highest thermal decomposition temperatures ranging from 309.7 to 458.0 °C. According to TGA analysis, the introduction of these substituents enhances thermal stability when compared with the **Model** compound (unsubstituted phthaloperinone) (T_d = 285.1 °C). As expected, the large, rigid and planar conjugated structure of pyrene substituent provides the highest thermal stability (T_d = 458 °C).[30] Additionally, it was also observed that the introduction of fluorine atoms (**3c**/**4c**) increases the thermal stability, comparing to compounds **3a**/**4a**, as C–F bond is one of the strongest bonds and, the inductive effect of fluorine atoms can reduce the likelihood of decomposition.[31] The introduction of an acetylene unit (–C≡C–) (**3d**/**4d**) also contributes to the increased thermal stability, probably due to extended conjugation and improved molecular packing.

On the other hand, compounds **3f**/**4f**, **3i**/**4i**–**3k**/**4k** exhibited lower thermal stability compared to the **Model** compound, possibly due to the non-planar nature of their substituents (as in compounds **3f**/**4f** and **3i**/**4i**), which disrupts π-stacking and weakens intermolecular interactions, and the presence of alkyl chains (as in compounds **3j**/**4j** and **3k**/**4k**), which increases molecular flexibility, reducing rigidity and packing efficiency. The decomposition temperature of compounds **3l**/**4l** is very similar to that of the **Model** compound. Although the triazole moiety in **3l**/**4l** is electron-rich and thermally stable, it does not provide significant additional thermal stabilization to the core structure.

As depicted in Table 1 and Fig. S95 (SI), DSC analysis shows that the melting temperatures do not differ significantly, except for compounds **3b**/**4b**, **3e**/**4e**, **3g**/**4g** and **3j**/**4j**. No events were observed for compounds **3f**/**4f** and **3i**/**4i** in the temperature range used in these studies.

Electroluminescence properties

The electroluminescence properties of these emitters were assessed in simple organic light-emitting diode (OLED) structures, where the active layer was made of phthaloperinone derivatives deposited by thermal deposition under high vacuum. Again, all regioisomer mixtures were tested, with the exception of **3k**/**4k**, due to its oil-like consistency. The general device structure consisted of glass/ITO (100 nm)/PEDOT:PSS (40 nm)/active layer (60–70 nm)/Ca (40 nm)/Al (>70 nm), as shown in Fig. 9(a).

In general, the light-onset voltage (here defined as the voltage at which a minimum luminance of 10^{-2} cd m^{-2} is

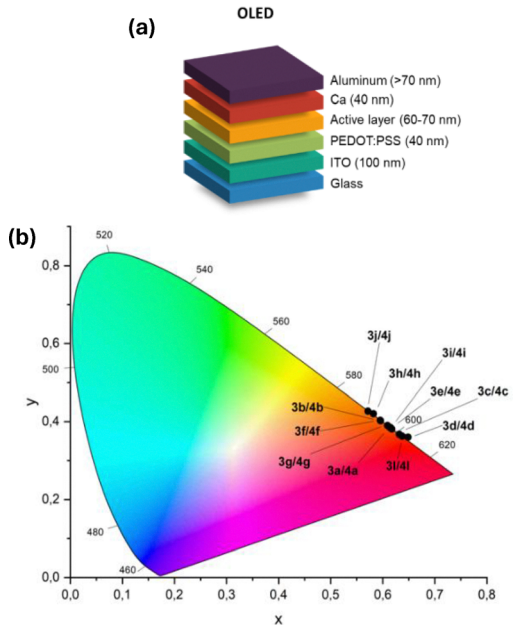

Fig. 9 (a) OLED device structures and (b) CIE (*x*,*y*) coordinates.

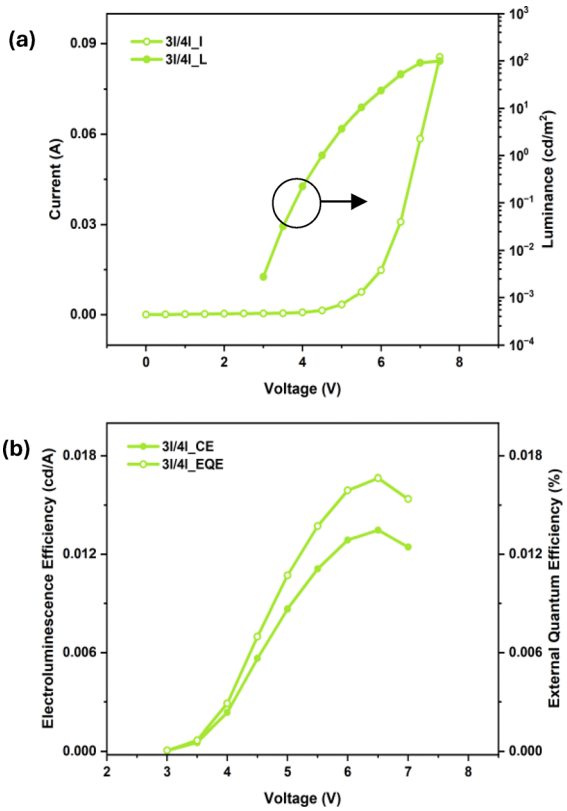

Fig. 10 (a) Current and luminance *versus* driving voltage of compounds **3l**/**4l**. (b) Electroluminescence efficiency and external quantum yield *versus* driving voltage of compounds **3l**/**4l**.

detected) varies significantly between compounds, ranging from 3.3 V (**3l**/**4l**) to 8.0 V (**3i**/**4i**) (Table S9 and Fig. S96, SI). Compounds **3c**/**4c**, **3d**/**4d**, **3f**/**4f** and **3h**/**4h** exhibited the poorest device performance, not even reaching a maximum luminance of 10 cd m^{-2} with very low current efficiency (<0.0015 cd A^{-1}). OLEDs based on compounds **3a**/**4a**, **3b**/**4b**, **3e**/**4e**, **3g**/**4g**, **3i**/**4i**, and **3j**/**4j** exhibited decent performances, with moderate maximum luminance (ranging from 11 to 41 cd m^{-2}) and low current efficiencies. Surprisingly, OLEDs based on compounds **3l**/**4l** achieved a maximum luminance of 99 cd m^{-2} at 7.5 V with a current efficiency of 0.014 cd A^{-1}. These compounds are also the ones that exhibit the lowest turn-on voltage (3.3 V). Therefore, OLEDs based on **3l**/**4l** show the best overall performance (Fig. 10(a)).

External quantum efficiencies (EQE) values vary in a very similar way to luminous efficiencies (Table S9 and Fig. S97, SI). Therefore, the highest EQE (0.017%) was also achieved with the OLEDs based on compounds **3l**/**4l** (Fig. 10(b)), which, surprisingly, are the compounds with the lowest solid and solution fluorescence quantum yield (Tables S5 and S6, SI). On the other hand, compounds with the higher solution fluorescence quantum yields (such as **3f**/**4f**, **3g**/**4g**, **3h**/**4h** and **3j**/**4j**) or powder fluorescence quantum yields (such as **3d**/**4d**) presented lower EQEs. As the radiative decay efficiency is expected to be the same under photoexcitation and under electrical excitation, the absence of proportionality between photoluminescence efficiency and electroluminescence efficiency is attributed to the different yields of excited state formation in the OLEDs, which is mainly determined by the charge (electrons and holes) mobility of the various compounds, as the charge injection barriers, in view of the similarity of the HOMO and LUMO energies, are expected not to vary much.

The performance of these simple OLEDs is comparable to previously reported devices based on PDI and NDI chromophores,[8–11] which is encouraging considering the simple device architecture employed. These results highlight the potential of phthaloperinone derivatives as efficient emitters and suggest that further optimization of the OLED architecture could lead to improved performance.

All phthaloperinone based OLEDs emit in the orange-red spectral region (Fig. 9(b)). The electroluminescence spectra (EL) are very similar for all compounds and are also similar to the photoluminescence spectra in solid-state (powder) (Table S10, SI). Similarly to the photoluminescence spectra in powder, EL spectra showed a red-shift when compared to the photoluminescence spectra in solution (Table S10, SI).

The shelf lifetime of OLEDs (structure shown in Fig. 9(a)) based on compounds **3c**/**4c**, **3e**/**4e**–**3j**/**4j** and **3l**/**4l** (Fig. S99, SI) was investigated. The aging studies were performed with the unfinished structure (without the top Ca/Al cathodes) in air/dark conditions or inside the glove box and characterised after the Ca/Al deposition. We found that the OLEDs incorporating compounds **3e**/**4e**, **3f**/**4f**, **3h**/**4h** and **3l**/**4l** did not exhibit significant changes in performance after aging for 5–17 days either in air/dark conditions or inside the glove box. Furthermore, the EL spectra of compounds **3e**/**4e**, **3f**/**4f** and **3l**/**4l** remained unchanged. On the other hand, OLEDs based on compounds **3g**/**4g** showed significant performance degradation after 17 days of aging, both in air/dark conditions and inside the glove box. The remaining OLEDs (those incorporating

compounds **3c**/**4c**, **3i**/**4i** and **3j**/**4j**) exhibited substantial and, in some cases, even complete loss of performance after nearly 100 days of aging under both conditions. Interestingly, the EL spectrum of the OLED containing compound **3i**/**4i** retained its spectral profile despite the performance loss. Only a few OLEDs produced detectable EL spectra, as the emission from most aged devices was too weak to allow their EL spectra to be recorded. Overall, OLEDs based on **3e**/**4e**, **3f**/**4f** and **3l**/**4l** appear to be the most stable.

Charge transport properties

Hole-only devices with the structure glass/ITO/PEDOT:PSS/compounds/MoO_3/Al were prepared with the intention of measuring hole-only current–voltage (*I*–*V*) characteristics of the same regioisomer mixtures (Fig. S100, SI). However, due to the reduced thickness of the active layer (60–70 nm), significant leakage currents were measured, which prevents accurate calculations of mobility values.

Despite this limitation, qualitative differences can still be observed among the devices. Differences in current levels and curve shapes suggest variations in charge transport efficiency, possibly influenced by the phthaloperinone derivatives' properties. For instance, the device based on compounds **3e**/**4e** showed higher current values when compared to compounds **3a**/**4a**, **3b**/**4b** and **3d**/**4d** in the negative voltage region indicating relatively better conduction behavior (Fig. S100(a), SI). While on the positive range, **3a**/**4a** exhibits the best result. Devices based on compounds **3f**/**4f**, and **3h**/**4h** exhibit increased current when compared to **3g**/**4g**, **3i**/**4i** and **3j**/**4j**, suggesting that these compounds may facilitate hole transport (Fig. S100(b), SI). Furthermore, when comparing compounds **3c**/**4c** and **3l**/**4l** it is possible to see that both devices display similar trends in the positive voltage range, with the exception of **3c**/**4c** which achieves higher currents in the negative voltage range (Fig. S100(c), SI).

Despite the limitations due to the thin active layer, which did not allow the determination of the hole mobility, these preliminary results provide insights into the relative charge transport properties of different compounds. For future studies, thicker active layers are needed to obtain reliable hole transport mobility values.

Conclusions

In this work, twelve novel phthaloperinone derivatives were synthesized and characterized. These compounds were designed at the molecular level to tune the photophysical, photochemical, electrochemical, thermal, and electronic properties of phthaloperinone – something that had never been done before with this structure.

A variety of substituents groups, with electron-donating and electron-withdrawing characteristics, were introduced to the phthaloperinone scaffold, and their impact was evaluated. DFT calculations revealed that compounds **3c**/**4c**, **3d**/**4d** and **3f**/**4f**–**3l**/**4l** caused interference in the eletronic charge distribution during the eletronic excitation process, while compounds with phenyl (**3a**/**4a**), naphthalene (**3b**/**4b**) and pyrene (**3e**/**4e**) aromatic units exhibited limited interaction with the phthaloperinone core. Additionally, based on predicted HOMO and LUMO energy levels, compounds **3f**/**4f**, which contain a triphenylamine group, emerged as the most promising organic semiconductive material. These theoretical predictions were supported by experimental photophysical and electrochemical studies. Overall, all synthesized derivatives demonstrated promising semiconductive properties, with compounds **3f**/**4f** exhibiting the lowest energy gap (2.22 eV).

Furthermore, electrochemical studies indicated that compounds **3e**/**4e**–**3h**/**4h** (bearing moderate and strong eletron donor substituents) and **3l**/**4l** (bearing phenyltriazolyl electron-withdrawing group) were shown to be the most stable, revealing reversibility in both negative and positive potential ranges. Thermal analysis revealed that compounds **3a**/**4a**–**3e**/**4e**, **3g**/**4g** and **3h**/**4h** showed increased thermal decomposition temperatures, *i.e.* increased thermal stability, when compared to that of the **Model** compound, with the pyrene-containing derivative (**3e**/**4e**) exhibiting the highest thermal stability (T_d = 458 °C).

In OLED devices, compounds **3e**/**4e**, **3g**/**4g**, **3i**/**4i** and **3j**/**4j** exhibited decent performances. However, compounds **3l**/**4l**, with a phenyltriazolyl unit, presented the best overall performance, achieving a maximum luminance of 99 cd m^{-2} at 7.5 V with a current efficiency of 0.014 cd A^{-1}. These compounds also exhibited the lowest turn-on voltage (3.3 V) and an EQE of 0.017%. These values, achieved using a simple device architecture, are comparable to those reported for PDI- and NDI-based systems, suggesting that further optimization of the device structure should yield even higher efficiencies.

Author contributions

ACA: writing – review & editing, writing – original draft, visualization, investigation, formal analysis and data curation. AJB: conceptualization, supervision, review & editing and resources. JM: investigation, supervision, review & editing, writing, investigation, formal analysis and resources. JPPR: investigation, writing, formal analysis, data curation and review & editing. HC: investigation, review & editing, writing, formal analysis and data curation. CC: investigation, formal analysis, writing and data curation. JAP: investigation, review & editing, writing and formal analysis. JSSM: investigation, supervision, review & editing, writing and formal analysis. LCB: review & editing, formal analysis and resources. SMML: consultation and technical assistance, review & editing.

Conflicts of interest

There are no conflicts to declare.

Data availability

The data supporting this article have been included as part of the supplementary information (SI). Supplementary information is available. See DOI: **https://doi.org/10.1039/d5ma00761e**.

CCDC 2423273 (**3b**) contains the supplementary crystallographic data for this paper.[32]

Acknowledgements

We thank the Fundação para a Ciência e a Tecnologia (FCT) for funding through the project 2022.01391.PTDC (ConChiMOL – New Structurally Contorted and Chiral Molecules for Optoelectronic Applications). We also acknowledge funding from the Coimbra Chemistry Centre (CQC), supported by the FCT through projects UIDB/00313/2025 and UIDP/00313/2025 (national funds), and the Institute of Molecular Sciences (IMS) (LA/P/0056/2020, DOI: 10.54499/LA/P/0056/2020) through special complementary funding from the FCT. Ana C. Amorim acknowledges the FCT for for the PhD Grant 2021.04769.BD. Addicional support was provided by FCT/MECI through national funds and, when applicable, co-funded EU funds under UID/50008: Instituto de Telecomunicações. The authors also acknowledge the financial support of the FCT, I.P.—within the scope of the projects UIDP/04449/2020 (HERCULES Lab), UIDB/04449/2020 (HERCULES Lab). This work was further financed by national funds from FCT/MCTES (Portugal) through Associate Laboratory for Green Chemistry–LAQV (LA/P/0008/2020 with DOI: 10.54499/LA/P/0008/2020, UIDP/50006/2020 with DOI: 10.54499/UIDP/50006/2020, and UIDB/50006/2020 with DOI: 10.54499/UIDB/50006/2020). Funding was also provided by FCT within the scope of the projects UIDB/04564/2020 and UIDP/04564/2020, with DOI identifiers 10.54499/UIDB/04564/2020 and 10.54499/UIDP/04564/2020, respectively. Carla Cunha thanks the FCT for a PhD Grant 2020.09661.BD. We gratefully acknowledge UC-NMR facility (**https://www.uc.pt/uc-nmr**) for all NMR analyses. We also acknowledge the Laboratório de Análises/REQUIMTE/LAQV for the acquisition of the TGA and DSC data. We thank Dr César Raposo and the Servicio de análisis elemental, cromatografía y masas for all mass spectroscopy analysis. Prof. Henrique Gomes is acknowledged for his advice on the semiconducting and other electronic aspects of these compounds.

References

1 P. Chen, J. Zhang, C. Yuan, X. Shao, H. Zhang and Z. Liu, *ChemPlusChem*, 2025, **90**, e202500301.
2 D. Zhou, L. Han, L. Hu, S. Yang, X. Shen, Y. Li, Y. Tong, F. Wang, Z. Li and L. Chen, *ACS Appl. Mater. Interfaces*, 2023, **15**, 8367–8376.
3 A. D. Hendsbee, J.-P. Sun, W. K. Law, H. Yan, I. G. Hill, D. M. Spasyuk and G. C. Welch, *Chem. Mater.*, 2016, **28**, 7098–7109.
4 J. D. Yuen, V. A. Pozdin, A. T. Young, B. L. Turner, I. D. Giles, J. Naciri, S. A. Trammell, P. T. Charles, D. A. Stenger and M. A. Daniele, *Dyes Pigm.*, 2020, **174**, 108014.
5 X. Xue, C. Li, K. Chenchai, X. Zhang, T. Shi, X. Zhang, G. Zhang and D. Zhang, *Macromol. Rapid Commun.*, 2025, e2400289.
6 S. Kang, J. Fan, J. B. P. Soares and M. Gupta, *RSC Adv.*, 2023, **13**, 5096–5106.
7 S. S. Birajdar, B. Mirka, V. K. Gawade, A. L. Puyad, B. H. Lessard, S. V. Bhosale and S. V. Bhosale, *Dyes Pigm.*, 2022, **206**, 110603.
8 S. V. Dayneko, M. Rahmati, M. Pahlevani and G. C. Welch, *J. Mater. Chem. C*, 2020, **8**, 2314–2319.
9 S. V. Dayneko, E. Cieplechowicz, S. S. Bhojgude, J. F. Van Humbeck, M. Pahlevani and G. C. Welch, *Mater. Adv.*, 2021, **2**, 933–936.
10 L. Zong, Y. Gong, Y. Yu, Y. Xie, G. Xie, Q. Peng, Q. Li and Z. Li, *Sci. Bull.*, 2018, **63**, 108–116.
11 H. F. Higginbotham, P. Pander, R. Rybakiewicz, M. K. Etherington, S. Maniam, M. Zagorska, A. Pron, A. P. Monkman and P. Data, *J. Mater. Chem. C*, 2018, **6**, 8219–8225.
12 K. I. Kobrakov, N. S. Zubkova, G. S. Stankevich, Yu. S. Shestakova, V. S. Stroganov and O. I. Adrov, *Fibre Chem.*, 2006, **38**, 183–187.
13 M. A. Faraonov, N. R. Romanenko, M. V. Mikhailenko, A. V. Kuzmin, S. S. Khasanov and D. V. Konarev, *New J. Chem.*, 2021, **45**, 13599–13607.
14 X. Zhang, T. Xu, Z. Tian, X. He, S. Zhang, L. Ai, W. Zhang, S. Liu and W. Song, *Chem. Commun.*, 2023, **59**, 5874–5877.
15 S. Dhami, Y. Kumar, C. Sengupta and R. Pandey, *Phys. Chem. Chem. Phys.*, 2023, **25**, 12363–12370.
16 C. A. Fernández-Gijón, F. del Río-Portilla, D. Ríos-Jara, S. Fomine, G. Santana and L. Alexandrova, *Tetrahedron*, 2015, **71**, 7063–7069.
17 S. Zhang, T. Xu, P. Wu, J. Pan, W. Zhang and W. Song, *J. Mater. Chem. C*, 2024, **12**, 4676–4681.
18 M. Mamada, C. Pérez-Bolívar and P. Anzenbacher, *Org. Lett.*, 2011, **13**, 4882–4885.
19 R. Loutfy, *Dyes Pigm.*, 1991, **15**, 139–156.
20 M. Mamada, C. Pérez-Bolívar, D. Kumaki, N. A. Esipenko, S. Tokito and P. Anzenbacher, *Chem. – Eur. J.*, 2014, **20**, 11835–11846.
21 M. Arai, M. Mori and Y. Nakaya, *Organic EL device*, US005981092A, 1999.
22 S. Goswami, D. Sen, N. K. Das and G. Hazra, *Tetrahedron Lett.*, 2010, **51**, 5563–5566.
23 J. R. Palmer, K. A. Wells, J. E. Yarnell, J. M. Favale and F. N. Castellano, *J. Phys. Chem. Lett.*, 2020, **11**, 5092–5099.
24 M. Łapkowski, *Materials*, 2021, **14**, 6880.
25 D. Cappello, F. L. Buguis and J. B. Gilroy, *ACS Omega*, 2022, **7**, 32727–32739.
26 M. J. Frisch, G. W. Trucks, H. B. Schlegel, G. E. Scuseria, M. A. Robb, J. R. Cheeseman, G. Scalmani, V. Barone, G. A. Petersson, H. Nakatsuji, X. Li, M. Caricato, A. V. Marenich, J. Bloino, B. G. Janesko, R. Gomperts, B. Mennucci, J. V. Hratchian, A. F. Ortiz, J. L. Izmaylov, D. Sonnenberg, F. Williams-Young, F. Ding, F. Lipparini, J. Egidi, B. Goings, A. Peng, T. Petrone, T. Henderson, D. Ranasinghe, V. G. Zakrzewski, J. Gao, N. Rega, G. W. Zheng, M. Liang, M. Hada, M. Ehara, K. Toyota, R. Fukuda, J. Hasegawa, M. Ishida, T. Nakajima, Y. Honda,

O. Kitao, H. Nakai, T. Vreven, K. Throssell, J. A. Montgomery Jr, J. E. Peralta, F. Ogliaro, M. J. Bearpark, J. J. Heyd, E. N. Brothers, K. N. Kudin, V. N. Staroverov, T. A. Keith, R. Kobayashi, J. Normand, K. Raghavachari, A. P. Rendell, J. C. Burant, S. S. Iyengar, J. Tomasi, M. Cossi, J. M. Millam, M. Klene, C. Adamo, R. Cammi, J. W. Ochterski, R. L. Martin, K. Morokuma, O. Farkas, J. B. Foresman and D. J. Fox, *Gaussian 16 Revision B.01*, Gaussian, Inc., Wallingford CT, 2016.

27 C. A. Guido, P. Cortona, B. Mennucci and C. Adamo, *J. Chem. Theory Comput.*, 2013, **9**, 3118–3126.

28 X. Song, S. Zhu, Y. Liu, T. Shi, L. Yang, Y. He, X. Niu, Z. Yang, J. Yuan and Z. Feng, *J. Mater. Chem. C*, 2024, **12**, 14129–14138.

29 M. Czichy, P. Janasik, R. Motyka, P. Zassowski, E. Grabiec, A. Wolinska-Grabczyk and M. Lapkowski, *Electrochim. Acta*, 2021, **370**, 137669.

30 R. Li, H. Xu, Y. Zhang, L. Chang, Y. Ma, Y. Hou, S. Miao and C. Wang, *RSC Adv.*, 2021, **11**, 39291–39305.

31 D. O'Hagan, *Chem. Soc. Rev.*, 2008, **37**, 308–319.

32 CCDC 2423273: Experimental Crystal Structure Determination, 2025, DOI: **10.5517/ccdc.csd.cc2mbm3q**.